

Machine-learning-accelerated design of high-performance platinum intermetallic nanoparticle fuel cell catalysts

Received: 4 July 2023

Accepted: 28 December 2023

Published online: 10 January 2024

Check for updates

Peng Yin^{1,3}, Xiangfu Niu^{2,3}, Shuo-Bin Li¹, Kai Chen², Xi Zhang¹, Ming Zuo¹, Liang Zhang²✉ & Hai-Wei Liang¹✉

Carbon supported PtCo intermetallic alloys are known to be one of the most promising candidates as low-platinum oxygen reduction reaction electrocatalysts for proton-exchange-membrane fuel cells. Nevertheless, the intrinsic trade-off between particle size and ordering degree of PtCo makes it challenging to simultaneously achieve a high specific activity and a large active surface area. Here, by machine-learning-accelerated screenings from the immense configuration space, we are able to statistically quantify the impact of chemical ordering on thermodynamic stability. We find that introducing of Cu/Ni into PtCo can provide additional stabilization energy by inducing Co-Cu/Ni disorder, thus facilitating the ordering process and achieving an improved tradeoff between specific activity and active surface area. Guided by the theoretical prediction, the small sized and highly ordered ternary Pt₂CoCu and Pt₂CoNi catalysts are experimentally prepared, showing a large electrochemically active surface area of ~90 m² g_{Pt}⁻¹ and a high specific activity of ~3.5 mA cm⁻².

Proton exchange membrane fuel cells (PEMFCs) with net-zero carbon emission are promising energy conversion devices^{1,2}, but the heavy use of high-cost platinum-based electrocatalysts for boosting the sluggish oxygen reduction reaction (ORR) at the cathode limits their large-scale commercialization^{3,4}. To this end, the US Department of Energy (DOE) has set two mass-normalized performance based on platinum group metal (PGM) as cost targets, including rated power (>8 kW g_{PGM}⁻¹) and activity (>0.44 A mg_{PGM}⁻¹)⁵. Hence, significant reduction of PGM usage by using ORR electrocatalysts with high mass activity (MA) is imperative to achieve full-commercialization of PEMFCs⁶.

Recently, carbon supported structurally ordered Pt-based intermetallic compound (IMC) nanoparticles have been extensively investigated as low-Pt catalysts to boost ORR for PEMFCs^{7–10}. Since the pronounced ordering-degree-dependent activity in intermetallic catalysts, the realization of high or even full ordering degree is highly desirable when preparing the alloy catalysts^{11,12}. To

promote the ordering degree of IMCs catalysts, high-temperature annealing is crucial to form the Pt-M alloys with ideal stoichiometric ratio and to overcome energy barrier of disorder-to-order transition within every individual nanoparticle¹³, which inevitably leads to the sintering of catalysts into larger particles with decreased electrochemical surface area (ECSA)^{14,15}. As demonstrated in a typical impregnation synthesis of PtCo alloy, the seesaw relation between particle size and ordering degree could be clearly observed (Fig. 1a). An acceptable MA of large-particle catalysts with a low ECSA could be achieved by the compensation of a very high SA^{16–18}. However, for a certain Pt usage in the membrane electrode assembly (MEA, mg_{Pt}/cm²_{MEA}), a low ECSA means a small Pt roughness factor in MEA (normalized ECSA on a cathode, cm²_{Pt}/cm²_{MEA}) that exacerbates the local oxygen transfer resistance, which eventually leads to a significantly decreased fuel cell performance, particularly at the high current density^{6,19}.

¹Hefei National Research Center for Physical Sciences at the Microscale, Department of Chemistry, University of Science and Technology of China, Hefei 230026, China. ²Center for Combustion Energy, School of Vehicle and Mobility, State Key Laboratory of Intelligent Green Vehicle and Mobility, Tsinghua University, Beijing 100084, China. ³These authors contributed equally: Peng Yin, Xiangfu Niu. ✉ e-mail: zhangbright@tsinghua.edu.cn; hwliang@ustc.edu.cn

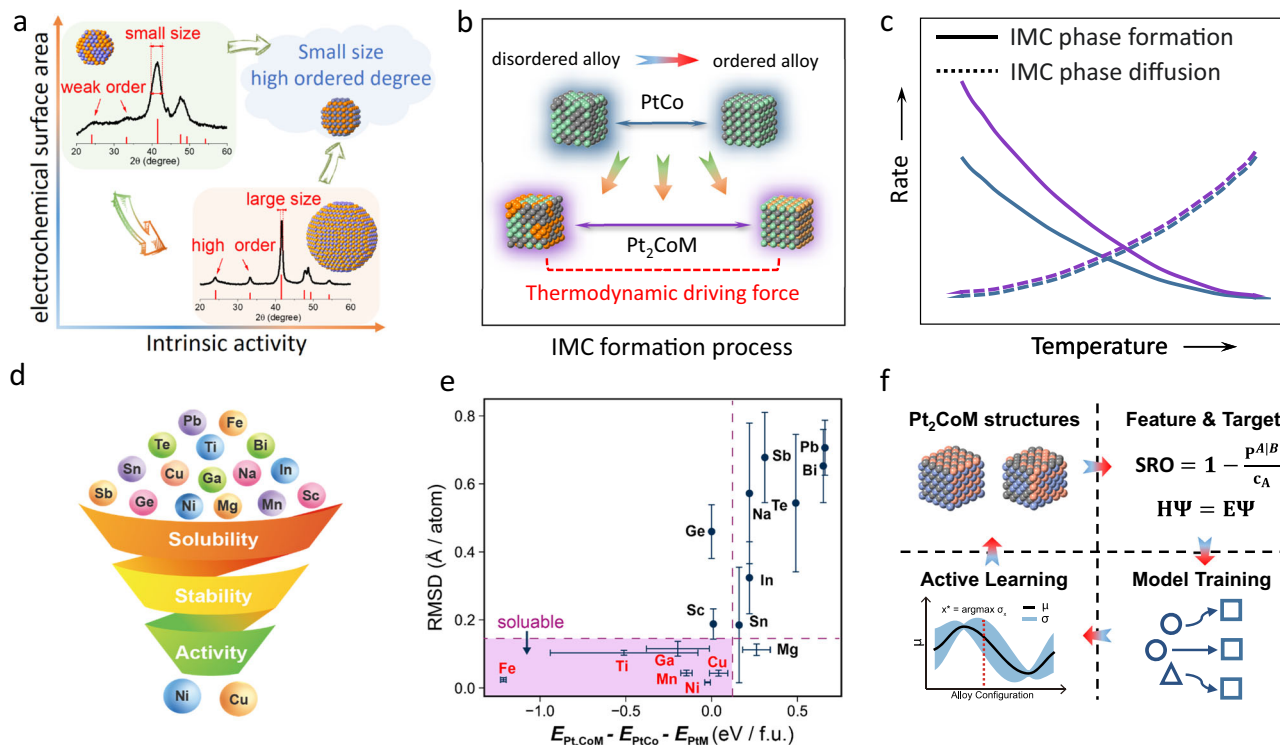


Fig. 1 | Development of machine learning model. **a** Schematic illustration showing the dilemma of ECSA and SA in a typical binary PtCo IMC catalyst synthesis. **b** Schematic illustration assuming the presence of Pt₂CoM combination with higher thermodynamic driving force of disordered-to-ordered transition. **c** Schematic illustration showing the change of IMC phase formation rate after

enhancing thermodynamic driving force. Purple and blue colors represent Pt₂CoM and PtCo, respectively. **d** Screening flowchart of ternary Pt₂CoM combinations. **e** Structural deformation and relative energy distribution of 16 Pt₂CoM combinations. **f** Active learning procedures to construct machine learning prediction model for relative energy of Pt₂CoM.

Some elaborately designed methods have been developed for preparing small-size Pt-based intermetallic catalysts, such as KCl matrix-assisted annealing²⁰, low temperature chemical vapor deposition with organometallic precursors²¹, sulfur-anchoring synthesis⁸, small-molecule assisted synthesis²², and thermal decomposition of bimetallic complexes²³. These methods focus on the anti-sintering during the high-temperature annealing; the ordering degree of the resulted IMCs catalysts is often low, even though the high kinetic energy barrier of atom ordering could be overcome by the high-temperature annealing. The reason behind this phenomenon is probably the low thermodynamic driving force in the disordered-to-order transition process^{13,15}, which would significantly limit the nucleation rate of IMC phase.

Recently, machine learning methods have demonstrated significant potential in accelerating material discovery by efficiently navigating design spaces and predicting properties, thereby substantially reducing the cost of identifying and optimizing catalytic materials^{24–27}. Here, we perform the machine-learning-accelerated computational screening, aiming at the de novo design of the element composition to increase the thermodynamic driving force for the disordered-to-order transition and thus promote the nucleation of IMC phase with high ordering degree (Fig. 1b, c). After the systematic screening of the ternary Pt₂CoM alloys (PtCo represents the most promising alloy catalyst for practical PEMFCs applications^{28,29}; M is another base metal element), including alloy mutual solubility, ordering transition energy, and strain-induced activity prediction, we obtain two optimal solutions of Pt₂CoCu and Pt₂CoNi. The experimentally prepared Pt₂CoCu (Ni) IMC catalysts show both large ECSA of $-90 \text{ m}^2 \text{ g}_{\text{Pt}}^{-1}$ and high SA of -3.5 mA cm^{-2} , which lead to a high MA of $-3 \text{ A mg}_{\text{Pt}}^{-1}$. The highly ordered Pt₂CoCu catalysts also exhibit enhanced MEA performance in practical H₂-air fuel cells.

Results and discussion

Computational screening of ternary Pt₂CoM alloys

To reduce the experimental trials and errors, we performed theoretical screening of the Pt₂CoM ternary system with the third element M from an initial pool of 16 potential elements, including Na, Mg, Sc, Ti, Mn, Fe, Ni, Cu, Ga, Ge, In, Sn, Sb, Te, Pb and Bi. The alloying of the third element aims to facilitate the Pt-M ordering while maintaining, if not enhancing the surface ORR performance. Therefore, the 16 candidates underwent screening in the following three aspects: solubility of M in PtCo alloy, promotion of a more feasible disorder-to-order transition in ternary Pt₂CoM compared to binary PtCo, and the potential for higher ORR activity in Pt₂CoM (Fig. 1d). Consequently, this systematic approach successfully narrowed down the potential ternary candidates to two: Pt₂CoCu and Pt₂CoNi, which were subsequently experimentally verified.

Figure 1e shows the two matrices used to assess the solubility of M in PtCo alloy: the relative energy of Pt₂CoM with respect to PtCo and PtM, and the structural deformation due to the M dissolving. For M=Fe, Ti, Ga, Mn, Ni, Cu, Sc, and Ge, the segregation of ternary Pt₂CoM to PtCo and PtM is thermodynamically unfavorable. However, it is important to note that even when segregation is thermodynamically preferred, the formation of a ternary alloy can still be kinetically stabilized. Meanwhile, Ge and Sc exhibit significant structural deformation after the density functional theory (DFT) optimization (Fig. 1e and Supplementary Fig. S1). Therefore, six soluble element Fe, Ti, Ga, Mn, Cu, and Ni, located in the left bottom of Fig. 1e were subjected to the ordering assessment in the next stage.

The activity and durability of Pt alloy catalysts are strongly dependent on the ordering degree of Pt and Co/M^{11,12}. Warren-Cowley short range order (SRO) was used to quantify the chemical ordering of the alloy system. We defined the ordering energy E_{ordering} as the energy

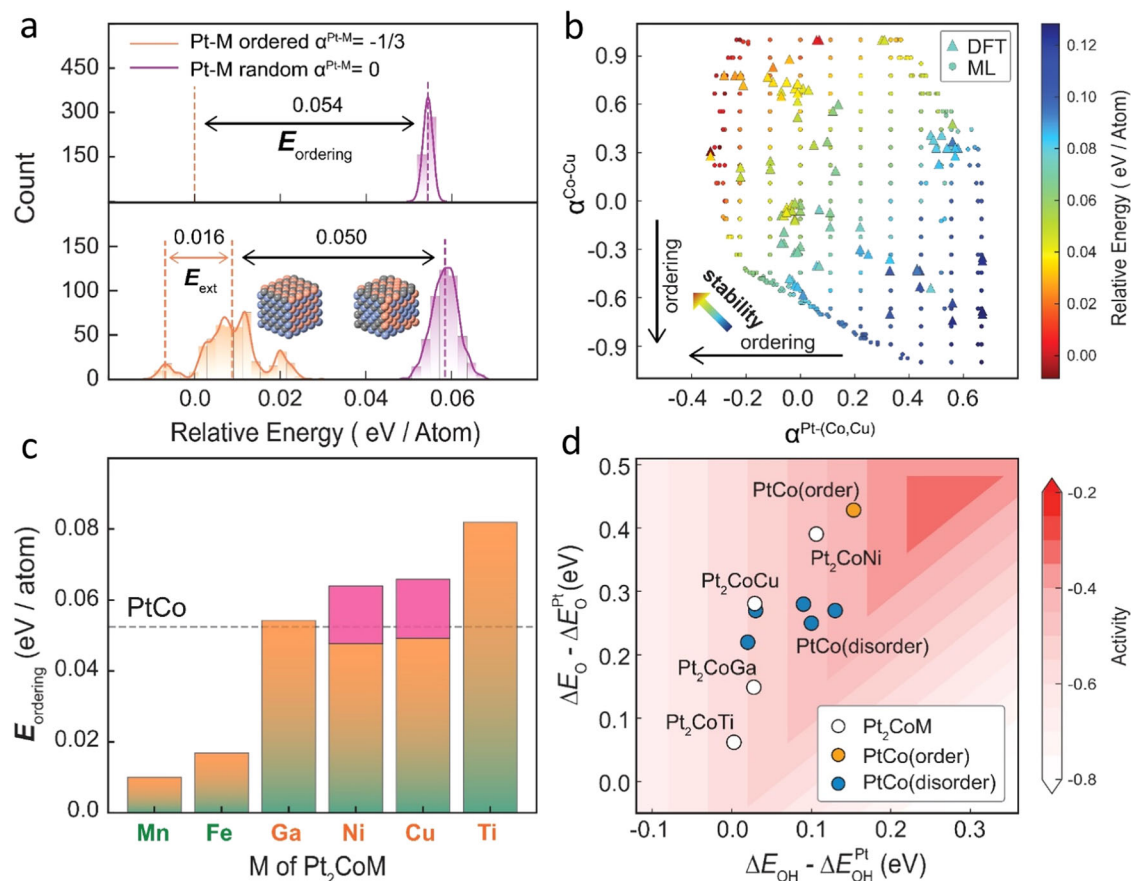


Fig. 2 | Result feedback of machine learning model. **a** ML predicted relative energies distribution of random and ordered PtCo (upper) and Pt₂CoCu (bottom). **b** Relative energies of Pt₂CoCu configurations as a function of Pt-Co/Cu SRO $\alpha^{\text{Pt-(Co/Cu)}}$ and Co-Cu SRO $\alpha^{\text{Co-Cu}}$. A higher SRO value represents a higher disordered degree. Triangles and circles represent data points computed by DFT (1 configurations per data point) and ML (average of 20 configurations for each data

point) prediction model, respectively. **c** Ordering energy E_{ordering} for six soluble Pt₂CoM combinations. Dashed line represents E_{ordering} of PtCo for reference. Red part represents the extra stabilization energy from the Co/Cu disordering. **d** ORR activity volcano plot of four ordered Pt₂CoM, ordered PtCo and five disordered PtCo.

difference between ordered configurations (SRO of Pt-Co/M: $\alpha^{\text{Pt-(Co/M)}} = -1/3$, where Pt atoms hold the same positions as PtCo intermetallics) and randomly mixed configurations ($\alpha^{\text{Pt-(Co/M)}} = 0$). The ordering energy E_{ordering} measures the thermodynamic driving force for the disorder-to-order transition. To overcome the intractability of the diverse interatomic arrangements in Pt₂CoM using DFT calculation, an active learning strategy was adopted to train the prediction model of relative energy for each Pt₂CoM ternary system (Fig. 1f and Supplementary Table S1). We selected Gaussian Process Regression (GPR) as the machine learning model due to its ability for uncertainty measurement²⁴. Active learning was implemented, and after completing 7 rounds of iterations, over 100 DFT data points were used for each Pt₂CoM, resulting in a formation energy prediction accuracy with an error below 10 meV/Atom (Supplementary Figs. S2–S5, Supplementary Table S2). The trained machine learning model was then applied to predict the formation energies of 300 ordered ($\alpha^{\text{Pt-(Co/M)}} = -1/3$) and 300 random ($\alpha^{\text{Pt-(Co/M)}} = 0$) configurations, as well as 3800 structures with varying ordering degrees (Supplementary Fig. S6). We found that the ordered PtCo was 0.054 eV per atom more stable than the configurations where Pt and Co were randomly mixed (upper panel of Fig. 2a). The introduction of Cu exhibits a similar thermodynamic barrier between the mean formation energy of ordered and random configurations (0.050 eV per atom). Interestingly, we found an extra small peak bringing an extra stabilization energy $E_{\text{ext}} = 0.016$ eV per atom for the Pt-Co/Cu ordered structure. Further analysis demonstrates that the extra stabilization energy of the

Pt-M ordering originates from the Co/Cu disordering (red section in Fig. 2c), where the relative formation energy of Pt₂CoCu increases with $\alpha^{\text{Pt-(Co/Cu)}}$, but oppositely correlates with $\alpha^{\text{Co-Cu}}$ (Fig. 2b and Supplementary Figs. S7 and S8). Similarly, we identified that Ga, Ni, Ti held the potential to form more ordered IMC structure, but the introduction of Mn and Fe would significantly suppress the thermodynamic driving force for the disorder-to-order transition of Pt₂CoM (Fig. 2c and Supplementary Table S1). In the realm of computational efficiency, the training and predicting with machine learning models required negligible time compared to DFT calculations, leading to a significant reduction in the time required to establish the correlation between chemical ordering and stability (Supplementary Fig. S9).

When catalyzing ORR, the Pt alloy catalysts should be converted into alloy@Pt core-shell structures by in situ electrochemical dealloying or pre-leaching in acid¹¹. The electronic properties of the Pt-shell are strongly influenced by the alloy core due to the well-known ligand and/or strain effects^{30,31}. To evaluate the ORR activity of the Pt₂CoM (M = Ga, Ni, Cu and Ti), we calculated the adsorption energies of OH* and O* as the activity descriptor using Pt-shell slab models with ordered Pt₂CoM-core (Fig. 2d and Supplementary Tables S3 and 4)³². The computed results show that strain effects play a dominated role in regulating the ORR activity of Pt₂CoM (Supplementary Fig. S10). For comparison, we also marked the calculated activity of ordered and disordered PtCo with various ordering degree of subsurface PtCo core. Generally, ordered PtCo possesses higher activity than disordered counterpart. Among the ternary alloys, Pt₂CoCu and Pt₂CoNi show

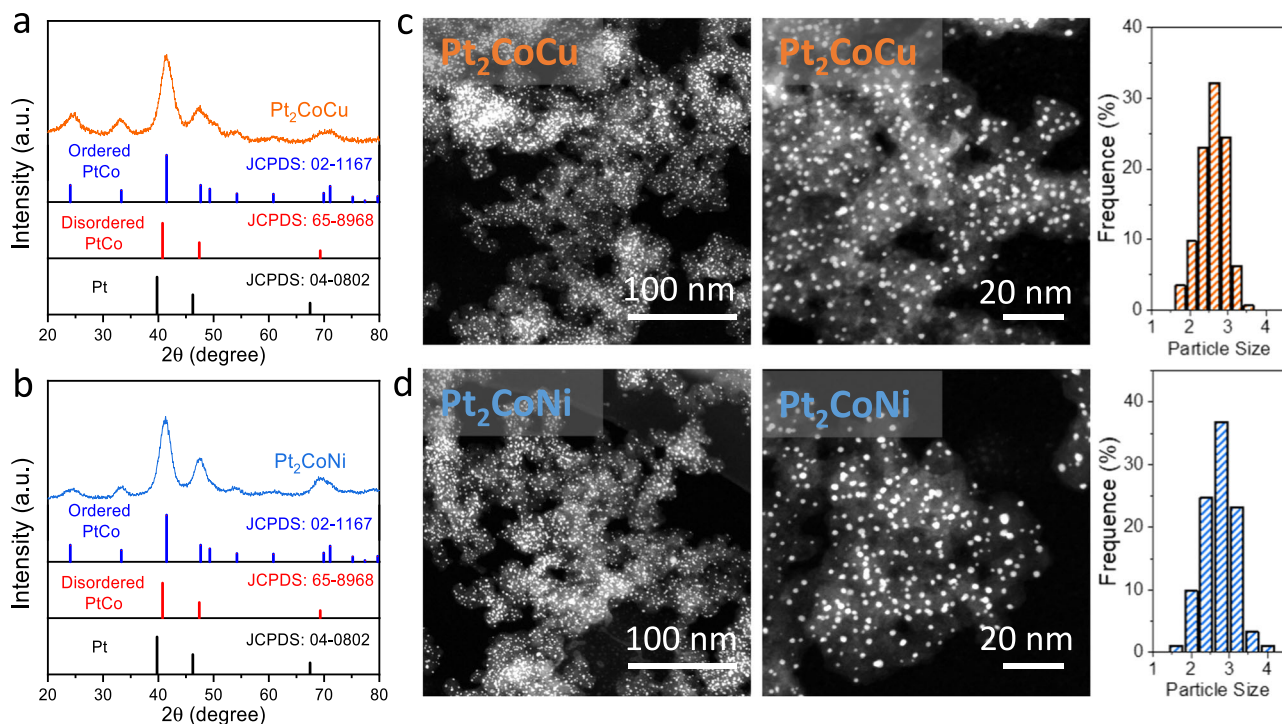


Fig. 3 | Synthesis of Pt₂CoCu/Pt₂CoNi IMC catalysts. XRD patterns of Pt₂CoCu (a) and Pt₂CoNi (b) catalysts. HAADF-STEM images and corresponding particle size distribution of Pt₂CoCu (c) and Pt₂CoNi (d) catalysts.

comparable ORR activity with fully ordered PtCo, and thus were finally selected for the experimental validation. There has been prior research reporting PtCoNi and PtCoCu ternary system as excellent ORR catalyst due to their near-optimum strain levels for higher ORR activity^{33,34}, aligning well with our computational screening results. More importantly, our study provides an innovative design perspective that the introduction of Cu/Ni leverages the thermodynamic driving force for the disordered-to-order transition, resulting in a more favorable tradeoff between specific activity (SA) and electrochemically active surface area (ECSA).

Synthesis and characterizations of Pt₂CoCu/Pt₂CoNi catalysts

The Pt₂CoCu and Pt₂CoNi catalysts were synthesized by the wet-impregnation of H₂PtCl₆ and corresponding non-noble metal salts on a carbon support Black Pearl 2000, followed by a high-temperature annealing at 1000 °C. We first performed the powder X-ray diffraction (XRD) characterizations to verify the L1₀-type intermetallic structures by comparing with the standard Powder Diffraction File cards of corresponding IMC (Fig. 3a, b). Different from a face-centered cubic structure in disordered PtCo alloy, two characteristic super-lattice peaks at around 24° and 33° were found in the Pt₂CoCu and Pt₂CoNi samples, indicating the formation of the L1₀ structures. After Rietveld refinement of the XRD patterns, we could obtain the fitting parameters for each diffraction peak (Supplementary Fig. S11 and Supplementary Table S5). In addition, the (111) peaks showed obvious broadening and no phase separation, suggesting a uniform IMC phase and small crystallite size. The average crystallite sizes calculated by the Debye-Scherrer equation based on the full-width at half-maximum of (111) peak were 2.94 nm and 3.19 nm for Pt₂CoCu and Pt₂CoNi, respectively.

High-angle annular dark-field scanning transmission electron microscopy (HAADF-STEM) revealed that Pt₂CoCu/Pt₂CoNi IMC nanoparticles were homogeneously distributed over the whole carbon matrix and no obvious aggregates or overgrowth of nanoparticles were found in both low- and high-resolution view fields (Fig. 3c, d). Statistical analyses suggested a narrow particle size distribution of Pt₂CoCu/Pt₂CoNi catalysts in the range of 1.5–4 nm, with average size

of 2.62 and 2.73 nm, respectively, which were close to the values estimated by XRD. Further, energy dispersive spectroscopy (EDS) elemental mapping with a large visual field indicated the homogeneous distributions of Pt and other non-noble metal elements in individual nanoparticles without element segregation (Fig. 4a, b).

We then performed aberration-corrected HAADF-STEM with atomic resolution to verify the ordered structure of the Pt₂CoCu/Pt₂CoNi catalysts (Fig. 4c, d). Owing to the atomic number (Z)-contrast differences between Pt and non-noble metals in an ordered lattice, the periodic regularity of brightness could be found along the specific zone axis; the Pt atoms will appear brighter than other non-noble metals with lower Z-contrast. Through their Z-contrast and atomic radius after local amplification, we could observe an alternating bright and dark stacking of Pt and non-noble metal columns. Our theoretical predictions suggested that Co with Cu or Ni tends to exhibit random site occupation. However, distinguishing the Co/Cu or Co/Ni position in the alloy structure is challenging due to their similar atomic radius³³. Fast Fourier transform (FFT) patterns further confirmed the face-centered tetragonal ordered structures of the Pt₂CoCu/Pt₂CoNi catalysts (Fig. 4c, d).

Electrochemical Performance

We first evaluated the ORR activity of the catalysts by the rotating disk electrode (RDE) technique. For comparison, we also prepared binary PtCo catalysts by the identical wet-impregnation method. Two types of PtCo catalysts, including the high-ordered/large-sized one (PtCo^{*}) and the low-ordered/small-sized one (PtCo[#]), were obtained at high-temperature and low-temperature annealing condition, respectively (Fig. 1a). As expected, the high-ordered/large-sized PtCo catalyst exhibited a higher intrinsic activity with SA of ~3.4 mA cm⁻² but a much lower ECSA of 15 m²g_{pt}⁻¹ than that of the low-ordered/small-sized catalyst (SA: 1.67 mA cm⁻²; ECSA: 87 m²g_{pt}⁻¹) (Fig. 5a and Supplementary Table S6). The trade-off relation between SA and ECSA makes the binary PtCo catalyst showing a limited mass activity (MA) of lower than 2.0 A mg_{pt}⁻¹ (Fig. 5b). In contrast, the high-ordered/small-sized ternary Pt₂CoCu/Pt₂CoNi catalysts broke such trade-off

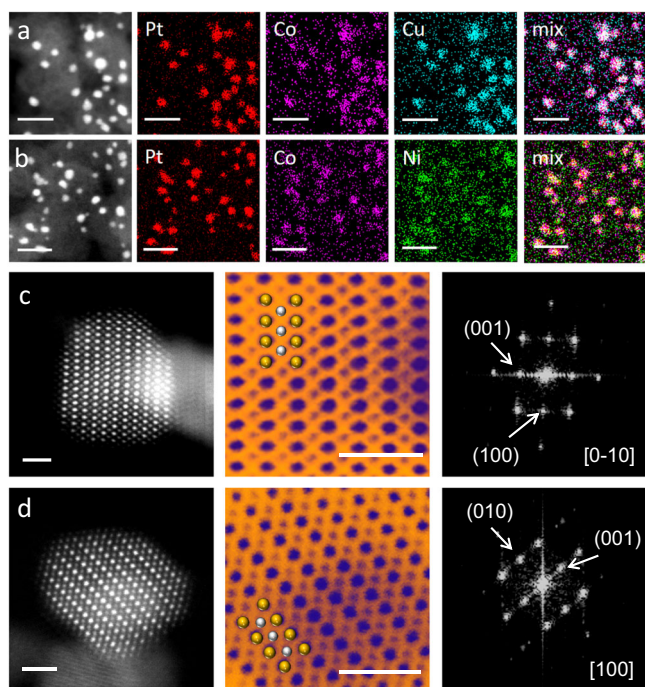


Fig. 4 | Structure characterization. EDS elemental mappings of the Pt₂CoCu (a) and Pt₂CoNi (b) catalysts, scale bar 10 nm. Atomic-resolution HAADF-STEM images and FFT patterns of Pt₂CoCu (c) and Pt₂CoNi (d) catalysts. Yellow balls represent Pt and silver balls represent CoCu (Ni). Scale bar: 1 nm.

relation, simultaneously showing a high SA ($\sim 3.5 \text{ mA cm}^{-2}$) and ECSA ($\sim 90 \text{ m}^2 \text{ g}_{\text{Pt}}^{-1}$), thus leading to a large MA of $\sim 3.0 \text{ A mg}_{\text{Pt}}^{-1}$. Moreover, after 30 K accelerated durability test (ADT) by cycling the potential between 0.6 and 0.95 V in RDE, the Pt₂CoCu/Pt₂CoNi catalysts showed a drop of 17.1% and 19.2% in the MA, along with a decrease of 10.2% and 22.2% in the SA (Fig. 5c, d and Supplementary Fig. S12). It has been well known that an IMCs@Pt core-shell structure would be formed in acid electrolytes and the Pt-shell could stabilize M against leaching to guarantee the durability under harsh voltage conditions^{30,35}.

We further evaluated the PEMFC performance of the Pt₂CoCu IMCs catalysts under practical H₂-air conditions. Prior to PEMFCs tests, the pristine IMCs catalysts were subjected to acid leaching and low-temperature H₂-annealing to form active and stable Pt-IMCs@Pt core-shell structures^{8,11}. EDS elemental mapping indicated the successful formation of core-shell structure with a Pt-rich shell (Fig. 6a). Atomic resolution HAADF-STEM and corresponding intensity profiles clearly verified an L1₀ intermetallic core surrounded by a Pt shell with three atomic layers (Fig. 6b). Low Pt loadings of $0.056 \text{ mg}_{\text{Pt}} \text{ cm}^{-2}$ and $0.020 \text{ mg}_{\text{Pt}} \text{ cm}^{-2}$ were adopted for the Pt₂CoCu IMCs cathode and the commercial Pt/C anode, respectively. For comparison, commercial Pt/C was also tested as the cathode catalyst with a loading of $0.100 \text{ mg}_{\text{Pt}} \text{ cm}^{-2}$. The low-Pt-loading Pt₂CoCu IMCs cathodes displayed high peak power densities of $\sim 1.1 \text{ W cm}^{-2}$ at $150 \text{ kPa}_{\text{abs}}/80 \text{ }^\circ\text{C}$, which were comparable to that of Pt/C cathode at a nearly double Pt loading (Fig. 6c). The enhanced power performance of the Pt₂CoCu IMC catalyst in high-current-density region ($>1.5 \text{ A cm}^{-2}$) was attributed to the advantage of high ECSA in minimizing mass-transport losses³⁶.

We finally evaluated the durability of the Pt₂CoCu and Pt/C cathodes from two metrics, voltage loss at 0.8 A cm^{-2} and MA. After a

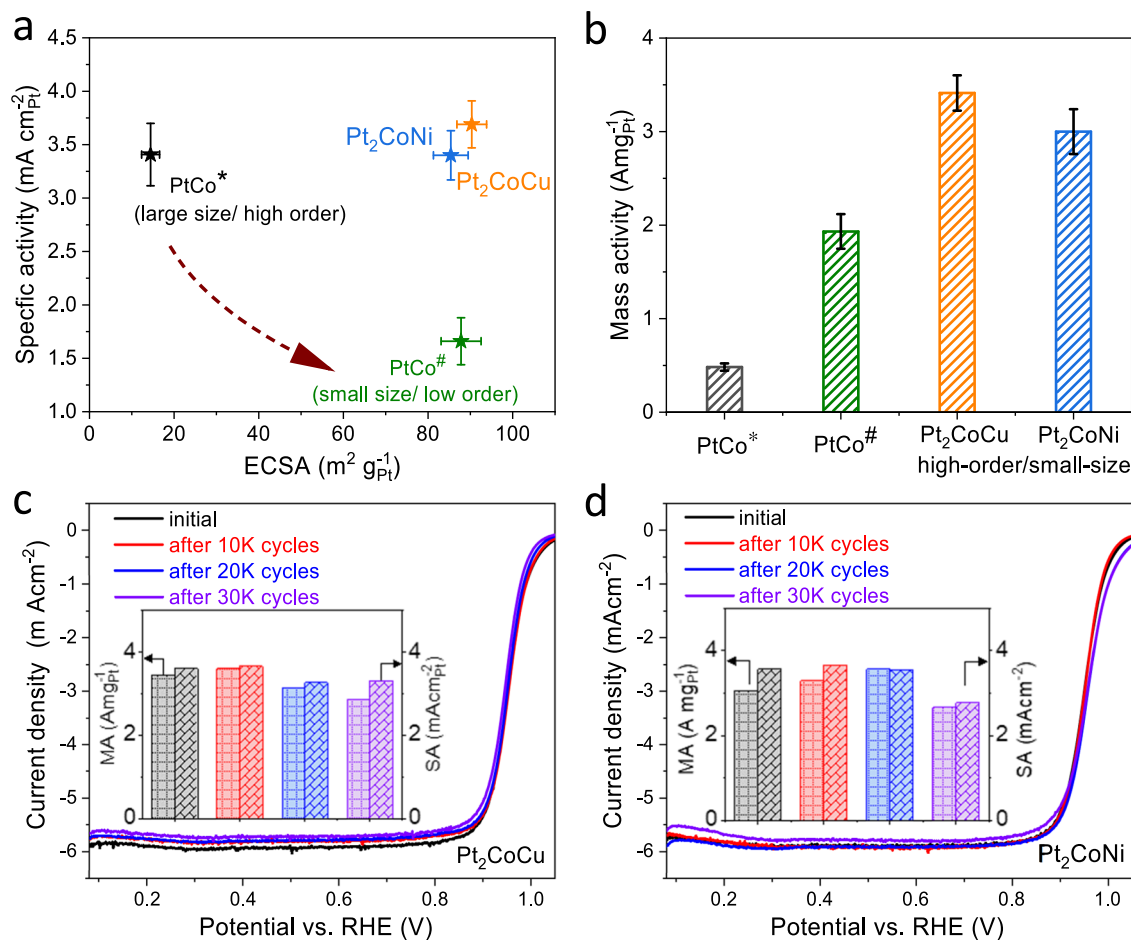


Fig. 5 | RDE performance. a, b Comparison of ECSA, SA, and MA of PtCo*, PtCo#, Pt₂CoCu, and Pt₂CoNi catalysts. ORR polarization curves and MA/SA loss of Pt₂CoCu (c) and Pt₂CoNi (d) catalysts after 30 K ADT.

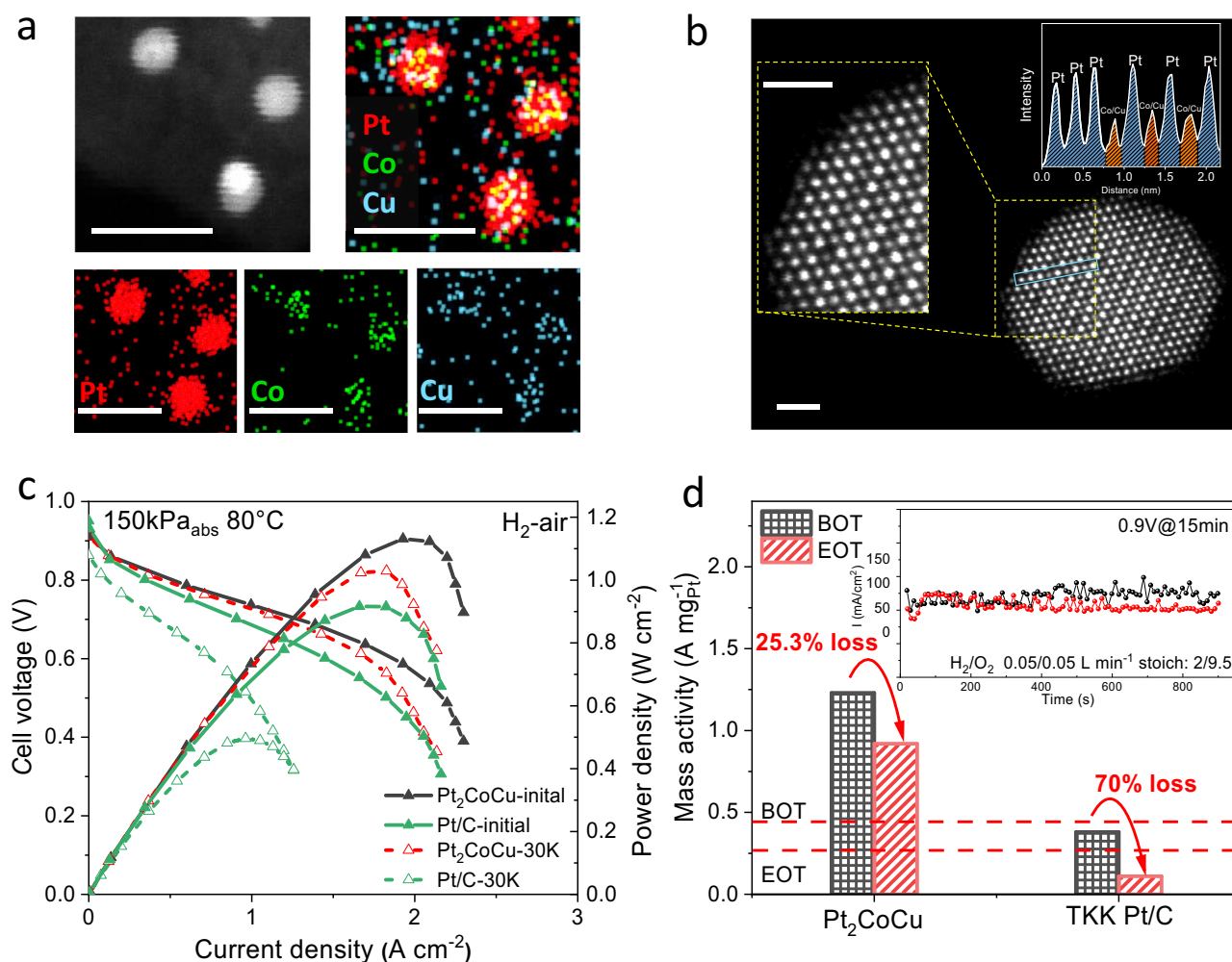


Fig. 6 | Fuel cell performance. **a** EDS elemental mappings of Pt₂CoCu@Pt core-shell structures. Scale bar: 10 nm. **b** Atomic resolution HAADF-STEM images and intensity profiles showing an intermetallic core with a thin Pt shell. Scale bar: 1 nm. **c** H₂/air polarization plots/power density plots before and after 30 K square wave

ADT. Test conditions: H₂/air 0.5/2 L min⁻¹, 80 °C, 100% relative humidity, 150 kPa_{abs}. **d** The loss of MA of EOT and BOT. Test conditions: H₂/O₂ 0.05/0.05 L min⁻¹, 80 °C, 100% relative humidity, 150 kPa_{abs}.

standard ADT protocol of a square wave potential cycling between 0.60 and 0.95 V (3-second hold at each voltage) suggested by US DOE (Supplementary Fig. S13), the current/power polarization plots at the beginning of test (BOT) and at the end of test (EOT) were obtained (Fig. 6c). The voltage loss for the Pt₂CoCu cathode at 0.8 A cm⁻² was 17 mV, which was much lower than the Pt/C cathode (-137 mV loss). Considering the instability of current in the high voltage region, DOE recommends multi-point test at 0.9 V_{iR-free} for 15 min under a low cathode stoichiometry of 9.5, and the MA was calculated based on the average current density at the last 1 min (Fig. 6d). The Pt₂CoCu IMC catalyst retained 74.7% of its BOT-MA, which was much higher than Pt/C (30% MA retention) and exceeded the DOE target (less than 40% loss with an BOT MA of 0.44 A mg_{Pt}⁻¹).

In summary, aided by the machine-learning-accelerated computational screening, we established an experiment-theory-collaborative design strategy of small-sized and highly ordered IMC catalysts for fuel cells. Thanks to the well-defined ordered structures of IMC in atomic level, a better concordance between experiment and machine learning simulation can be guaranteed, which makes it feasible to quickly discover potential IMC combinations with high thermodynamic driving force for the disorder to order transition from the enormous design space. Computationally, we found that alloying Cu/Ni promoted the formation of IMC due to the additional stabilization energy introduced

by the Co-Cu/Co-Ni disordering. Experimental results demonstrated that the ternary Pt₂CoCu/Pt₂CoNi IMC catalysts could achieve the compatibility of small size (thus high ECSA) and high ordering degree (thus high SA), and finally achieved much improved mass-normalized performance in practical fuel cells.

Methods

DFT Calculation

All DFT calculations were performed using Vienna Ab Initio simulation packages (VASP)³⁷. The interaction between the core and valence electrons was treated using projected-augmented wave (PAW) method³⁸. A kinetic energy cutoff of 400 eV was used for the plane-wave basis set. The exchange-correlation energy was evaluated by the Perdew-Burke-Ernzerhof (PBE) functional at the generalized gradient approximation (GGA) level³⁹. The energy tolerance of 5×10^{-5} eV was used in electronic structure calculations, and the geometry optimization was performed until all force was less than 0.03 eV Å⁻¹. The unit cell of PtCo in P4/mmm space group was downloaded from Material Project⁴⁰. To construct the unit cell for Pt₂CoM, (M is the third element doped to PtCo), the unit cell of PtCo was repeated twice and a Co atom was replaced by an M atom. The lattice constants of all Pt₂CoM unit cells were re-optimized by DFT. To analyze the solubility and disorder-to-order transition energy of Pt₂CoM, a (3 × 3 × 3) supercell was

constructed based on the DFT optimized Pt₂CoM unit cell. Atomic arrangement of initial Pt₂CoM supercell was shuffled to generate configurations with different ordering degrees. A (3 × 3 × 3) Monkhorst-Pack k-point grid was utilized to sample the Brillouin zone for the supercell model⁴¹. To analyze the activity of Pt₂CoM, the close-packed Pt₂CoM (111) surfaces were simulated by a five-layer (4 × 4) slab model, in which two Pt₂CoM bottom layers were fixed and three Pt skin layers added on them were allowed to relax. Activity of ordered PtCo were evaluated using three Pt-skin layers with two ordered PtCo-core layers. The arrangement of Pt and Co in the ordered PtCo-core were shuffled to generate disordered PtCo slab models. A vacuum layer of 7.5 Å was added above and below the slab to avoid periodic interactions. A (4 × 4 × 1) Monkhorst-Pack k-point grid was employed to sample the Brillouin zone for slab model. The spin polarization was included in the calculation of slab model for Fe, Co and Ni. The adsorption energy of O and OH were calculated by the following Equations:

$$\Delta E_{\text{O}} = E_{\text{O}^*} - E_{\cdot} - (E_{\text{H}_2\text{O}} - E_{\text{H}_2}) \quad (1)$$

$$\Delta E_{\text{OH}} = E_{\text{OH}^*} - E_{\cdot} - (E_{\text{H}_2\text{O}} - 1/2E_{\text{H}_2}) \quad (2)$$

where the E_{\cdot} , E_{O^*} and E_{OH^*} are DFT calculated energies for clean surface, surface with O and OH, respectively. The $E_{\text{H}_2\text{O}}$ and E_{H_2} are energies of H₂O and H₂ are -6.76 eV and -14.22 eV respectively, which are calculated by DFT using a H₂O and H₂ molecule placed on a 10 Å × 10 Å × 10 Å cubic cell model. The adsorption Gibbs free energy was defined by:

$$\Delta G = \Delta E + \Delta E_{\text{water}} + \Delta \text{ZPE} - T\Delta S \quad (3)$$

Where ΔE_{water} is the solvation correction, ΔZPE is the zero point correction and $T\Delta S$ is the entropic correction, in this work we used correction values from the reference³².

Short Range Order. The Warren-Cowley short range order is defined as Eq. (4)⁴²:

$$\alpha^{X-Y} = 1 - \frac{P^{X|Y}}{C_X} \quad (4)$$

where X and Y denote two kinds of alloy elements, C_X is the ratio of element X, $P^{X|Y}$ is the probability of finding X in the neighbor shell of Y. At a fixed C_X , a negative $\alpha^{X|Y}$ value suggests the preference for forming X-Y bond, which is characteristic of an ordered alloy; on the contrary, a positive α^{X-Y} value demonstrates the segregation of X and Y; and α^{X-Y} value close to 0 represents a random alloy configuration. Here the configurations with the lowest short range order value $\alpha^{\text{Pt}-(\text{Co}/\text{M})} = -1/3$ are defined as order alloy, and configurations with $\alpha^{\text{Pt}-(\text{Co}/\text{M})} = 0$ are regarded as random alloy.

Solubility Test

The initial 16 candidate elements include alkali metal Na; alkaline-earth metal Mg; 3d transition metals Sc, Ti, Mn, Fe, Ni, Cu; P-block elements Ga, Ge, In, Sn, Sb, Te, Pb, Bi. Given that the lowest and highest values of $\alpha^{\text{Pt}-(\text{Co}/\text{M})}$ for the Pt₂CoM supercell model are -1/3 and 2/3 respectively, as depicted in Supplementary Fig. S6. 22 Pt₂CoM structures with different ordering degrees were generated (four structures for each $\alpha^{\text{Pt}-(\text{Co}/\text{M})} = -1/6, 0, 1/6, 2/6$ and 3/6, one structure for $\alpha^{\text{Pt}-(\text{Co}/\text{M})} = -2/6, 4/6$). Monte Carlo algorithm was applied to generate structures with the given $\alpha^{\text{Pt}-(\text{Co}/\text{M})}$ value by manipulating the arrangement of Pt, Co and M in Pt₂CoM supercell model. Geometry optimizations were then conducted by DFT on these structures. Root mean square deviation (RMSD) was used to quantify the structural deformation during the

geometry optimizations, RMSD is defined as:

$$\text{RMSD} = \frac{1}{n} \sqrt{\sum_{i=1}^n (X'_i - X_i)^2} \quad (5)$$

where n is the total number of atoms in the supercell model, X'_i and X_i are the positions of i-th atom before and after geometry optimization.

Machine Learning

Machine learning (ML) model was trained to replace DFT calculation to predict the energy for given alloy configuration. Extracting features from alloy structure as the input of ML model based on domain knowledge is of great importance for rationalizing the prediction model. Given that the stability of Pt₂CoM exhibits a strong correlation with the ordering degree (Supplementary Fig. S8), 15-dimensional numerical fingerprints reflecting the ordering degree of alloy configurations were designed and applied as the input of the ML model. The features consist of two parts. The Warren-Cowley short range order defined by three kinds of diatomic pairs (Pt-Co, Pt-M and Co-M) in three neighboring shells were used, which constituted the first nine dimensions in the feature. In addition, numbers of different diatomic bond pairs (Pt-Co, Pt-M, Co-M, Pt-Pt, Co-Co, M-M) were the other six dimensions for the feature. To avoid unbalanced weighting due to the different value ranges of each dimension in the feature, the original features were standardized to have a mean of 0 and a standard deviation of 1. Furthermore, to remove the redundant features and reduce calculation demands, principal component analysis (PCA) was carried out and only the principal components with a proportion of variance 99% were reserved. The DFT calculated relative energy of Pt₂CoM (energy reference to ordered Pt₂CoM supercell model) was used as the output for the ML model.

The Gaussian Process Regression (GPR) model was selected as the machine learning model by taking advantage of its ability for uncertainty measurement⁴³. Gaussian process regression is a non-parametric Bayesian inference regression technique. Unlike traditional regression method, Gaussian Process Regression gives a posterior distribution rather than exact value for the prediction target. Gaussian Process can be regarded as an infinite Gaussian distribution, and each final random variables set of Gaussian Process obeys a multivariate normal distribution, which can be denoted by:

$$f(X) \sim N(\mu(X), K(X)) \quad (6)$$

where $X = (x_1, x_2, \dots, x_n)$ is a set of random variables, $f(X)$ is the target properties, $\mu(X)$ is mean of target properties, $K(X)$ is the covariance matrix. For the new datapoint x^* needed to be predicted, the union set of X and x^* also obey following multivariate normal distribution:

$$\begin{bmatrix} f(X) \\ f(x^*) \end{bmatrix} \sim N \left(\begin{bmatrix} \mu(X) \\ \mu(x^*) \end{bmatrix}, \begin{bmatrix} K(X) & K(X, x^*)^T \\ K(X, x^*) & K(x^*, x^*) \end{bmatrix} \right) \quad (7)$$

The posterior distribution of $f(x^*)$ can be calculated by maximizing the likelihood function, and the results are expressed as following:

$$f(x^*) \sim N(\mu(x^*), \sigma(x^*)) \quad (8)$$

$$\mu(x^*) = K(X, x^*)^T K(X)^{-1} f(X) \quad (9)$$

$$\sigma(x^*) = K(x^*, x^*) - K(X, x^*)^T K(X)^{-1} K(X, x^*) \quad (10)$$

The scikit-learn package was used for constructing GPR model⁴⁴. Each term in the covariance matrix indicate the covariance between

two elements, which was defined by the radial-basis function (RBF):

$$k(x, x') = C^2 \exp\left(-\frac{(x - x')^2}{2l^2}\right) \quad (11)$$

where C and l are scale factor and length factor, respectively. During the ML model training process, values of C and l were optimized to maximize the log-marginal-likelihood. The values range of C^2 and l^2 is limited to between 10^{-5} and 10^3 , and 50 independent optimizations were conducted to avoid local optimums.

Active Learning

The workflow of active learning is shown in Supplementary Fig. S2. The uncertainty given by trained GPR model was used as the criterion to select samples in next generation. Due to the difficulty of exhausting the alloy configuration space, Monte Carlo simulation was performed to search the Pt₂CoM configuration with the high prediction uncertainty. Starting from a randomly initialized structure, Monte Carlo optimization controls the evolution of the structure along the high uncertainty direction through changing the atomic arrangement. When the uncertainty of the new structure is higher than that of the previous structure, the new structure was accepted; when the uncertainty of the new structure is lower than that of the previous structure, the new structure was accepted with a certain probability. In addition, to avoid getting trapped in local optimums, 20 simulations were performed and the first 10 structures with the highest uncertainty were extracted. The newly searched 10 structures were labeled by DFT and added into the pre-existing dataset. Then the ML model was retrained using the extended database. Such an active learning iteration was repeated 7 times. The searched Pt₂CoCu configurations representing by their t-SNE in the active learning process was shown in Supplementary Fig. S3. The prediction accuracy of the ML model was measured using mean absolute error (MAE) and coefficient of determination (R²), where the 80% data was adopted as the training set and the remaining 20% data was the test set. The evolution of prediction accuracy in the active learning process are shown in Supplementary Figs. S4–5. The completed ML model was used to predict the energies of 300 ordered alloy structures and 300 random alloy structures.

Materials and Chemicals

Carbon black (Black Pearls 2000, BP2000) was produced by America Cabot Corporation. Commercial Pt/C (TEC10E20E) was purchased from TANAKA. All others chemicals were commercially available from Sinopharm Chemical Reagent Co. Ltd., China, including chloroplatinic acid (H₂PtCl₆·6H₂O), cobalt chloride hexahydrate (CoCl₂·6H₂O), copper chloride dehydrate (CuCl₂·2H₂O), nickel chloride hexahydrate (NiCl₂·6H₂O), ethanol, and isopropanol. All the chemicals were used as received without further purification. DI water (18.2 MΩ/cm) used in all experiments was prepared by passing through an ultra-pure purification system.

Catalysts preparation

The Pt₂CoCu and Pt₂CoNi IMC catalysts were prepared with the BP2000 carbon black support by a conventional impregnation method that involved the wetness impregnation of metal salt and subsequent thermal reduction in 5% H₂/Ar. Taking the synthesis of Pt₂CoCu for an example, 50 mg BP2000, 20 mg H₂PtCl₆·6H₂O, 6.4 mg CoCl₂·6H₂O, and 3.9 mg CuCl₂·2H₂O was first mixed in a 100 mL round-bottom flask containing 40 mL DI water. After stirring overnight, the mixture was subjected to ultrasonic treatment for 2 h before drying by using a rotary evaporator. Finally, the dried powder was transferred to a tube furnace and thermally reduced at 1000 °C under flowing 5% H₂/Ar for 2 h.

RDE Measurements

The Pt₂CoCu (Ni) IMC catalysts were assessed for their ORR activity using the RDE techniques using a CHI Electrochemical Station (Model 760E) in a three-electrode cell. The catalyst ink, comprising 4 mg of catalyst and 40 μL of Nafion in 2 mL of isopropanol, was prepared through sonication. Then, the ink was applied via drop-coating onto the working electrode, a 5.0 mm diameter glassy carbon disk, and left to air-dry at room temperature. Reference and counter electrodes were provided by saturated Hg/HgSO₄ and a platinum plate, respectively. All potentials in this study were referenced to the reversible hydrogen electrode (RHE) for each test. The catalyst underwent activation using cyclic voltammetry (scan rates of 250 mV s⁻¹ and potential ranges of 0.05–1.05 V vs. RHE) until achieving a stable curve. Linear sweep voltammetry (LSV) measurements were then conducted in O₂-saturated 0.1 M HClO₄ solution, sweeping the potential from 0.05 to 1.05 V at a rate of 10 mV/s (1600 rpm). Mass activity calculations involved capacitance-correction and IR-correction. For accelerated durability tests (ADTs), the potential was cycled between 0.6 and 0.95 V at a rate of 100 mV s⁻¹ at room temperature under N₂-saturated 0.1 M HClO₄ solution. The electrochemical active surface area (ECSA) was determined through a CO stripping test. CO stripping test involved bubbling CO into 0.1 M HClO₄ electrolyte, holding potential at 0.05 V for 10 min, followed by bubbling N₂ into the electrolyte for 30 min. Subsequently, a cyclic voltammetry curve was recorded by scanning from 0.05 V to 1.05 V at a rate of 50 mV s⁻¹.

PEMFCs Tests

The catalysts first underwent acid treatment and subsequent annealing to create Pt-IMCs@Pt core-shell structures⁸, which aimed to mitigate the poison effect of leached metal cation during the fuel cell operation. A uniform ink was prepared by dispersing catalysts in a solvent blend of n-propanol and water (1:1), incorporating Aquivion D72-25BS ionomer at an ionomer/carbon ratio of 0.8. The ink concentration was maintained at 3 mg_{cat} mL⁻¹. The catalyst-coated-membrane was created by applying an ultrasonic spray (ExactaCoat FC, Sono-Tek Corporation) on a GORE Nafion membrane (12 μm, 5 cm²). A gas diffusion layer (GDL) was used Freudenberg (H24CX483, 235 μm) with a microporous layer. The membrane electrode assembly (MEA), incorporating two GDLs, two gaskets, and the prepared CCM, was assembled with a compression of 34%. The seven channel serpentine flow field was applied for the all single-cell tests (designed by Hubert Gasteger and co-workers⁴⁵), where the pressure drop between the inlet and outlet of the flow field was less than 10 kPa.

The MEA was made with the Pt₂CoCu (0.056 mg_{pt} cm⁻²) or benchmark Pt/C cathode (TEC10E20E, TANAKA, 0.1 mg_{pt} cm⁻²) and the commercial Pt/C anode with a Pt loading 0.02 mg_{pt} cm⁻². Initially, calibration curves were established to quantify the correlation between the number of spray cycles and catalyst loading. This approach allows the attainment of a specific Pt loading by adjusting the number of spraying cycles. The reproducibility of the instrument ensures the accuracy of each spraying.

The mass activity (MA) of MEA was assessed at 0.9 V_{IR-corrected}, 80 °C, 100% relative humidity, 150 kPa_{abs}, outlet H₂-O₂ at 0.05/0.05 L min⁻¹ flow rate (equivalent to the stoichiometry ratio of 2/9.5). A hold time of 15 min was implemented, and the mass activity calculated based on the average current during the last 1 min. The corresponding current was corrected for H₂ crossover. The H₂-air performance of single cell was conducted at 80 °C, 100% relative humidity, 150 kPa_{abs}, outlet H₂-air at 0.5/2 L min⁻¹ flow rate. For comparison, MEA made with Pt/C cathodes with a loading of 0.1 mg_{pt} cm⁻² were also measured. According to the US DOE ADT protocol for PGM-based catalysts on carbon-based supports, the accelerated durability test (ADT) for the MEA involved applying a square wave voltage from 0.6 to 0.95 V, lasting 3 seconds at each voltage level. Each test was run up to 30,000

cycles at 80 °C, 100% RH, with H₂/N₂ flow 200/75 sccm for the anode and cathode, respectively.

Characterization

XRD were performed on a Japan Rigaku DMax-γA rotation anode x-ray diffractometer equipped with graphite monochromatized Cu-K radiation. HAADF-STEM images were produced on FEI Talos F200X operated at 200 kV. Atomic resolution HAADF-STEM images were produced on probe aberration-corrected JEM ARM200F (S) TEM operated at 200 kV. EDS mapping were used FEI Talos F200X equipped with Super X-EDS system.

Data availability

All source data for DFT modeling and machine learning that were used in this study are available from the GitHub repository: <https://github.com/ZhangLabTHU/PtCoM>. Source data are provided with this paper.

References

- Banham, D. & Ye, S. Current status and future development of catalyst materials and catalyst layers for proton exchange membrane fuel cells: an industrial perspective. *ACS Energy Lett.* **2**, 629–638 (2017).
- Yarlagadda, V. et al. Boosting fuel cell performance with accessible carbon mesopores. *ACS Energy Lett.* **3**, 618–621 (2018).
- Pollet, B. G., Kocha, S. S. & Staffell, I. Current status of automotive fuel cells for sustainable transport. *Curr. Opin. Electrochem.* **16**, 90–95 (2019).
- Kongkanand, A. & Mathias, M. F. The priority and challenge of high-power performance of low-platinum proton-exchange membrane fuel cells. *J. Phys. Chem. Lett.* **7**, 1127–1137 (2016).
- US Department of Energy, Multi-Year Research, Development, and Demonstration Plan, https://www.energy.gov/sites/default/files/2017/05/f34/cto_myrd_d_fuel_cells.pdf (2017).
- Kodama, K., Nagai, T., Kuwaki, A., Jinnouchi, R. & Morimoto, Y. Challenges in applying highly active Pt-based nanostructured catalysts for oxygen reduction reactions to fuel cell vehicles. *Nat. Nanotechnol.* **16**, 140–147 (2021).
- Chong, L. et al. Ultralow-loading platinum-cobalt fuel cell catalysts derived from imidazolate frameworks. *Science* **362**, 1276–1281 (2018).
- Yang, C.-L. et al. Sulfur-anchoring synthesis of platinum intermetallic nanoparticle catalysts for fuel cells. *Science* **374**, 459–464 (2021).
- Escudero-Escribano, M. et al. Tuning the activity of Pt alloy electrocatalysts by means of the lanthanide contraction. *Science* **352**, 73–76 (2016).
- Antolini, E. Alloy vs. intermetallic compounds: Effect of the ordering on the electrocatalytic activity for oxygen reduction and the stability of low temperature fuel cell catalysts. *Appl. Catal. B Environ.* **217**, 201–213 (2017).
- Li, J. et al. Hard-Magnet L10-CoPt Nanoparticles Advance Fuel Cell Catalysis. *Joule* **3**, 124–135 (2018).
- Song, T. W. et al. Intermetallic PtFe Electrocatalysts for the Oxygen Reduction Reaction: Ordering Degree-Dependent Performance. *Small* **18**, 2202916 (2022).
- Zeng, W.-J. et al. Phase diagrams guide synthesis of highly ordered intermetallic electrocatalysts: separating alloying and ordering stages. *Nat. Commun.* **13**, 7654 (2022).
- Li, J. & Sun, S. Intermetallic nanoparticles: synthetic control and their enhanced electrocatalysis. *Acc. Chem. Res.* **52**, 2015–2025 (2019).
- Yan, Y. et al. Intermetallic nanocrystals: Syntheses and catalytic applications. *Adv. Mater.* **29**, 1605997 (2017).
- Li, M. et al. Ultrafine jagged platinum nanowires enable ultrahigh mass activity for the oxygen reduction reaction. *Science* **354**, 1414–1419 (2016).
- Chen, C. et al. Highly crystalline multimetallic nanoframes with three-dimensional electrocatalytic surfaces. *Science* **343**, 1339–1343 (2014).
- Zhang, L. et al. Platinum-based nanocages with subnanometer-thick walls and well-defined, controllable facets. *Science* **349**, 412–416 (2015).
- Wang, X. X., Swihart, M. T. & Wu, G. Achievements, challenges and perspectives on cathode catalysts in proton exchange membrane fuel cells for transportation. *Nat. Catal.* **2**, 578–589 (2019).
- Chen, H. et al. A surfactant-free strategy for synthesizing and processing intermetallic platinum-based nanoparticle catalysts. *J. Am. Chem. Soc.* **134**, 18453–18459 (2012).
- Choi, D. S., Robertson, A. W., Warner, J. H., Kim, S. O. & Kim, H. Low-temperature chemical vapor deposition synthesis of Pt–Co alloyed nanoparticles with enhanced oxygen reduction reaction catalysis. *Adv. Mater.* **28**, 7115–7122 (2016).
- Song, T. W. et al. Small molecule-assisted synthesis of carbon supported platinum intermetallic fuel cell catalysts. *Nat. Commun.* **13**, 6521 (2022).
- Yoo, T. Y. et al. Scalable production of intermetallic Pt–Co electrocatalyst for high-power proton-exchange-membrane fuel cell. *Energ. Environ. Sci.* **16**, 1146–1154 (2023).
- Wang, Y. et al. Fundamentals, materials, and machine learning of polymer electrolyte membrane fuel cell technology. *Energy AI* **1**, 100014 (2020).
- Mou, T. et al. Bridging the complexity gap in computational heterogeneous catalysis with machine learning. *Nat. Catal.* **6**, 122–136 (2023).
- Zhong, M. et al. Accelerated discovery of CO₂ electrocatalysts using active machine learning. *Nature* **581**, 178–183 (2020).
- Back, S., Tran, K. & Ulissi, Z. W. Toward a design of active oxygen evolution catalysts: insights from automated density functional theory calculations and machine learning. *ACS Catal.* **9**, 7651–7659 (2019).
- Konno, N., Mizuno, S., Nakaji, H. & Ishikawa, Y. Development of compact and high-performance fuel cell stack. *SAE Int. J. Altern. Pow.* **4**, 123–129 (2015).
- Takahashi, T. et al. Accelerated durability testing of fuel cell stacks for commercial automotive applications: A case study. *J. Electrochem. Soc.* **169**, 044523 (2022).
- Bu, L. et al. Biaxially strained PtPb/Pt core/shell nanoplate boosts oxygen reduction catalysis. *Science* **354**, 1410–1414 (2016).
- Strasser, P. et al. Lattice-strain control of the activity in dealloyed core-shell fuel cell catalysts. *Nat. Chem.* **2**, 454–460 (2010).
- Nørskov, J. K. et al. Origin of the overpotential for oxygen reduction at a fuel-cell cathode. *J. Phys. Chem. B* **108**, 17886–17892 (2004).
- Li, J. et al. Anisotropic Strain Tuning of L10 Ternary Nanoparticles for Oxygen Reduction. *J. Am. Chem. Soc.* **142**, 19209–19216 (2020).
- Hu, B. et al. High activity and durability of a Pt–Cu–Co ternary alloy electrocatalyst and its large-scale preparation for practical proton exchange membrane fuel cells. *Compos. Part B Eng.* **222**, 109082 (2021).
- Wang, D. et al. Structurally ordered intermetallic platinum–cobalt core-shell nanoparticles with enhanced activity and stability as oxygen reduction electrocatalysts. *Nat. Mater.* **12**, 81–87 (2013).
- Ahn, C. Y. et al. Differences in the Electrochemical Performance of Pt-Based Catalysts Used for Polymer Electrolyte Membrane Fuel Cells in Liquid Half- and Full-Cells. *Chem. Rev.* **124**, 15075–15140 (2021).
- Kresse, G. & Furthmüller, J. Efficient iterative schemes for ab initio total-energy calculations using a plane-wave basis set. *Phys. Rev. B* **54**, 11169 (1996).
- Kresse, G. & Joubert, D. From ultrasoft pseudopotentials to the projector augmented-wave method. *Phys. Rev. B* **59**, 1758 (1999).

39. Perdew, J. P., Burke, K. & Ernzerhof, M. Generalized gradient approximation made simple. *Phys. Rev. Lett.* **77**, 3865 (1996).
40. Jain, A. et al. Commentary: The Materials Project: A materials genome approach to accelerating materials innovation. *APL Mater.* **1**, 011002 (2013).
41. Monkhorst, H. J. & Pack, J. D. Special points for Brillouin-zone integrations. *Phys. Rev. B* **13**, 5188 (1976).
42. Owen, L., Playford, H., Stone, H. & Tucker, M. A new approach to the analysis of short-range order in alloys using total scattering. *Acta Mater.* **115**, 155–166 (2016).
43. Deringer, V. L. et al. Gaussian process regression for materials and molecules. *Chem. Rev.* **121**, 10073–10141 (2021).
44. Pedregosa, F. et al. Scikit-learn: Machine learning in Python. *J. Mach. Learn. Res.* **12**, 2825–2830 (2011).
45. Simon, C., Hasche, F., Muller, D. & Gasteiger, H. A. Influence of the Gas Diffusion Layer Compression on the Oxygen Mass Transport in PEM Fuel Cells. *ECS Trans.* **69**, 1293–1302 (2015).

Acknowledgements

We acknowledge the funding support from the National Natural Science Foundation of China (Grants 22325903, 22221003, 22103047, 22305158, and 22071225), the National Key Research and Development Program of China (Grant 2018YFA0702001), the Plan for Anhui Major Provincial Science & Technology Project (Grants 202203a0520013 and 2021d05050006), the Joint Funds from Hefei National Synchrotron Radiation Laboratory (Grant KY2060000175), the China Postdoctoral Science Foundation (Grant 2022M722195 and 2023T160435) and USTC Research Funds of the Double First-Class Initiative (Grant YD2060002032).

Author contributions

H.-W.L., L.Z. and P.Y. conceived and designed the project. L.Z., X.N. and K.C. carried out the DFT calculations and machine learning. P.Y., S.-B.L. and X.Z. synthesized and characterized the catalysts. M.Z. performed the HAADF-STEM characterization. P.Y. and S.-B.L. performed electrochemical test. P.Y., X.N., L.Z. and H.-W.L. co-wrote the paper. All the authors discussed the results and commented on the manuscript.

Competing interests

The authors declare no competing interests.

Additional information

Supplementary information The online version contains supplementary material available at <https://doi.org/10.1038/s41467-023-44674-1>.

Correspondence and requests for materials should be addressed to Liang Zhang or Hai-Wei Liang.

Peer review information *Nature Communications* thanks the anonymous reviewer(s) for their contribution to the peer review of this work. A peer review file is available.

Reprints and permissions information is available at <http://www.nature.com/reprints>

Publisher's note Springer Nature remains neutral with regard to jurisdictional claims in published maps and institutional affiliations.

Open Access This article is licensed under a Creative Commons Attribution 4.0 International License, which permits use, sharing, adaptation, distribution and reproduction in any medium or format, as long as you give appropriate credit to the original author(s) and the source, provide a link to the Creative Commons license, and indicate if changes were made. The images or other third party material in this article are included in the article's Creative Commons license, unless indicated otherwise in a credit line to the material. If material is not included in the article's Creative Commons license and your intended use is not permitted by statutory regulation or exceeds the permitted use, you will need to obtain permission directly from the copyright holder. To view a copy of this license, visit <http://creativecommons.org/licenses/by/4.0/>.

© The Author(s) 2024